



# Flow control by leading edge prism cylinders for a wave energy harvesting turbine

P. Sadees<sup>1</sup> · Abdus Samad<sup>1</sup>

Received: 27 July 2023 / Accepted: 22 January 2024 / Published online: 8 March 2024  
© The Author(s), under exclusive licence to Springer Nature Switzerland AG 2024

## Abstract

Separated flow on a Wells turbine blade causes poor performance of the turbine. Implementing passive flow control techniques, such as leading-edge prism cylinders (LE-PCs), effectively delays flow separation within a system. The prism cylinder alters the angle of attack (AoA) and modifies the boundary layer profile. The shapes of the prism cylinders were square, hexagonal, octagonal, and decagonal. The prism cylinder circumference was fixed at 2% of the chord length ( $C$ ), and the gap between the PC and the LE was  $2.5\%C$  and  $3.5\%C$ . The prism cylinder was placed at the blade chord line to maintain the Wells turbine symmetry. For the numerical simulations, the turbine performance parameters are calculated using steady-state Reynolds-averaged Navier–Stokes (RANS) equations along with a  $k-\omega$  SST turbulence model. Results showed that a gap of  $3.5\%C$  of the hexagonal prism cylinder improves the performance and provides a more comprehensive working range of 22.22% and an average torque coefficient of 43%. The prism cylinder modifies vortex strength and kinetic energy of the incoming flow and, finally, manipulates the suction-surface (SS) flow separation and re-energizes the separated flow.

**Keywords** Prism cylinders · Wells turbine · CFD · Wave energy · OWC

## Abbreviations

CFD	Computational fluid dynamics
LE	Leading-edge
NACA	National Advisory Committee of Aeronautics
OWC	Oscillating water column
PC	Prism cylinder
PCAWT	Prism cylinder assisted Wells turbine
PS	Pressure side
PTO	Power take-off device
RANS	Reynolds-averaged Navier–Stokes
SS	Suction surface
SST	Shear stress transport
TKE	Turbulent kinetic energy ( $\text{m}^2/\text{s}^2$ )
TLF	Tip leakage flow
TLV	Tip leakage vortex

WEC

Wave energy converter

## Symbols

$C$	Chord length ( $m$ )
$C_p$	Static pressure drop coefficient (–)
$h = \frac{R_{\text{hub}}}{R_{\text{tip}}}$	Hub-to-tip ratio (–)
$K$	Specific turbulent kinetic energy ( $\text{m}^2/\text{s}^2$ )
$Q$	Airflow rate ( $\text{m}^3/\text{s}$ )
$R_{\text{hub}}$	Hub radius ( $m$ )
$R_{\text{tip}}$	Tip radius ( $m$ )
$T_t$	Total torque ( $\text{N m}$ )
$U_A$	Inlet axial velocity ( $\text{m/s}$ )
$U_{\text{tip}}$	Rotor tip velocity ( $\text{m/s}$ )
$\varepsilon$	Dissipation rate ( $\text{m}^2/\text{s}^3$ )
$P$	The density of air ( $\text{kg}/\text{m}^3$ )
$\Omega$	Rotational speed (rpm)
$\omega$	Specific turbulent dissipation rate ( $\text{s}^{-1}$ )
$\Delta p$	Stagnation pressure drop (Pa)
$T^* = \frac{T_t}{\rho \Omega^2 D_{\text{tip}}^3}$	Torque coefficient (–)
$U^* = \frac{U_A}{U_{\text{tip}}}$	Flow coefficient (–)

✉ Abdus Samad  
samad@iitm.ac.in

P. Sadees  
pg.sadees@gmail.com

<sup>1</sup> Wave Energy and Fluids Engineering Laboratory, Indian Institute of Technology Madras, Chennai, India

$$\Delta p^* = \frac{\Delta p}{\rho \Omega^2 D_{\text{tip}}^2} \quad \text{Pressure loss coefficient (-)}$$

$$\eta = \frac{T_i \Omega}{Q \Delta p} \quad \text{Efficiency (\%)}$$

## 1 Introduction

Recently global push for renewable energy has given momentum to harness energy from ocean waves. Several efforts are going on all over the world to harness such energy. On the other hand, the challenges to harness such energy are abundant. An oscillating water column (OWC) is the most commonly used device. OWC systems offer a promising solution for harnessing hydropower into electricity, particularly in areas with limited space. OWC systems are more compact than other energy conversion systems, making them ideal for installation in space-limited areas. The recent intensive investigations on OWC systems have led to the establishment of commercial-scale OWC plants, indicating their viability in practical hydropower applications (Barstow et al. 2007). OWC can be installed at the nearshore to extract the ocean's wave energy (Falcao 2010). The working principle of OWC systems is illustrated in Fig. 1, which comprises a water column, an air chamber, and a power take-off (PTO) unit. During exhalation, air compression within the chamber increases pressure, causing airflow towards the atmosphere and rotation of the turbine in the PTO unit connected to the electrical generator, thus converting pneumatic energy into electrical energy. On the other hand, during inhalation, the water level decreases, and the air chamber pressure is lowered, resulting in reverse airflow.

Several researchers have conducted a numerical analysis of the oscillating water column (OWC) system. (Falcão and Henriques 2016; Mahnamfar and Altunkaynak 2017; Moñino et al. 2017; Shalby et al. 2019; Opoku et al. 2023). The turbine unit's damping significantly influences the OWC system's overall efficiency (López et al. 2016). Air turbines, specifically the Wells and impulse turbines, are essential components of the OWC system. Among the air turbines studied in the OWC, the impulse turbine has been reported by multiple researchers. They have documented variations in the setting angle, tip clearance, number of blades, and optimization of guide vanes, as well as the thickness of the rotor blade and the addition of fillets on a blade (Hyun and Moon 2004; Thakker et al. 2004, 2005; Xiong and Liu 2011; Gomes et al. 2012; Badhurshah and Samad 2015; Liu et al. 2016; Maurya et al. 2022).

The Wells turbine's blade symmetry generates unidirectional torque, making it insensitive to incoming flow direction. Figure 2 shows the turbine's velocity triangle, where the tangential velocity ( $U_T$ ) causes blade rotation. The incoming axial and relative velocities ( $V$  and  $W$ ) are

denoted by subscripts 1 and 2 for flow inlet and exit. As the blade rotates, it achieves an acceptable angle of attack (AoA), enabling lift ( $F_L$ ) and drag force ( $F_D$ ) generation. The resolution of aerodynamic force components determines the total force in the axial ( $F_A$ ) and tangential ( $F_T$ ) directions. The tangential force remains constant direction, while the axial force changes direction based on incoming flow orientation. Increased tangential force enhances turbine output, but increased axial force reduces efficiency due to higher pressure drop. Lift increases to a critical value with an increase in the AoA, after which a stall occurs, decreasing the operating range (Raghunathan 1995). However, the Wells turbine is known to experience flow separation, which restricts its operational range. It is worth noting that the Wells turbine, introduced in 1970 by Alan A. Wells, is considered the first of its kind and has since gained wide recognition (Inoue et al. 1985; Raghunathan and Tan 1985; Gato et al. 1996; Setoguchi and Takao 2006). Its symmetric blade configuration ensures a constant direction of tangential force, regardless of the airflow direction, enabling consistency with unidirectional rotation (Thakker and Abdulhadi 2007). Unfortunately, this symmetry also results in stalling, sharply reducing the turbine's efficiency when airflow exceeds a critical value (Raghunathan 1995).

To overcome the challenges the OWC system faces, researchers have studied and identified various flow control methods. The Wells turbine's successful energy conversion depends on effectively managing flow separation. One approach to mitigate this is through active and passive flow control methods. Active techniques typically enhance a system's efficiency more significantly than passive ones (Amundarain et al. 2010; Greenblatt et al. 2021). Despite this, such methods often increase complexity and expenses, necessitating additional energy and components (Ceballos et al. 2015; Lekube et al. 2018). Passive control methods, which require minimal design modifications, can broaden the operating range of turbines. A commonly employed technique involves modifying the geometry of the blades to manipulate pressure distribution, thereby reducing flow separation. Researchers have utilized optimization algorithms to develop different blade profiles based on experimental and numerical data, increasing operating ranges (Mohamed et al. 2011; Shaaban 2017; Gratton et al. 2018).

Scientists have explored various methods to improve turbine performance and expand the operational range. One such approach is optimizing the blade sweep angle using an optimization method to enhance the torque coefficient (Halder et al. 2017). Another effective technique involves shifting the blade thickness towards the leading edge, providing higher efficiency and improving the stall margin at higher flow coefficients (Takao et al. 2006; Halder et al. 2018). Casing treatment presents a promising way to improve

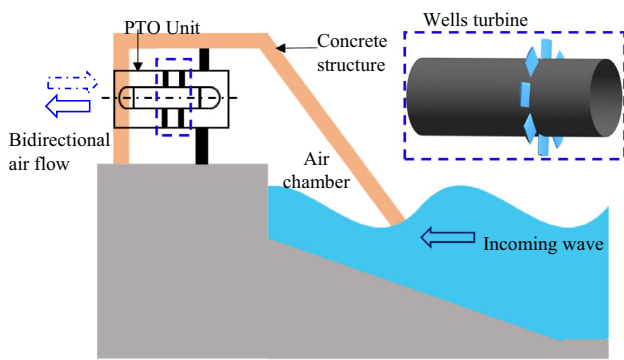


**Fig. 1** Shore-based OWC schematic representation with Wells turbine

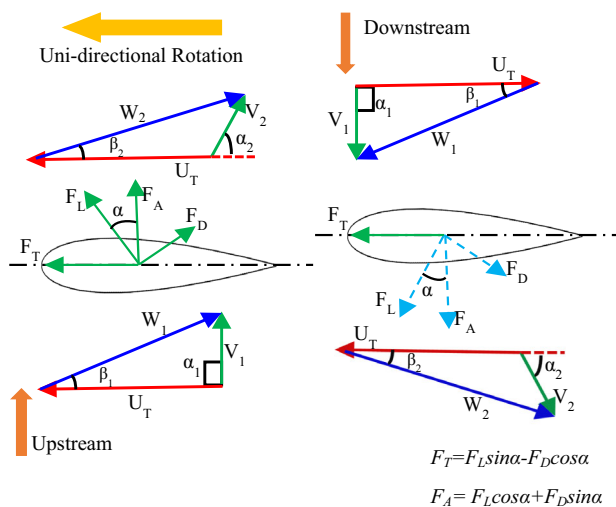


**Fig. 2** Aerodynamic forces acting on Wells turbine

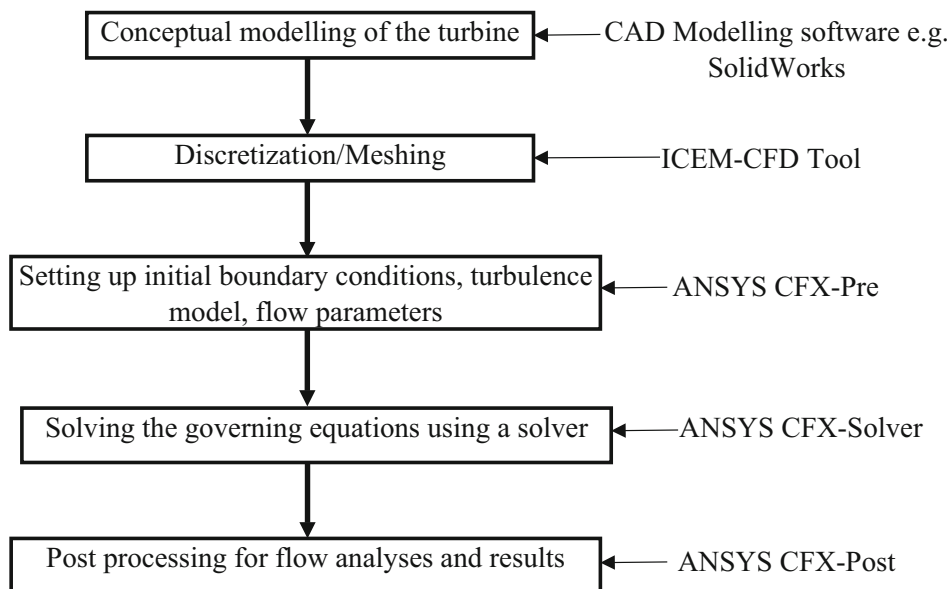
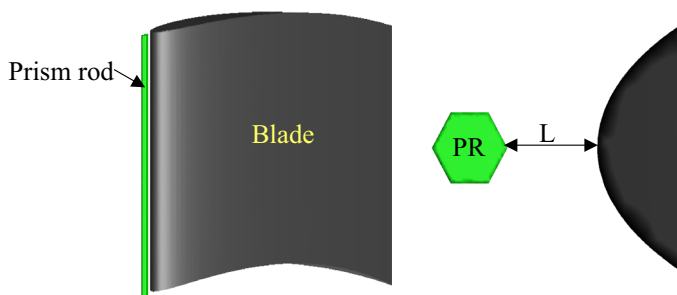
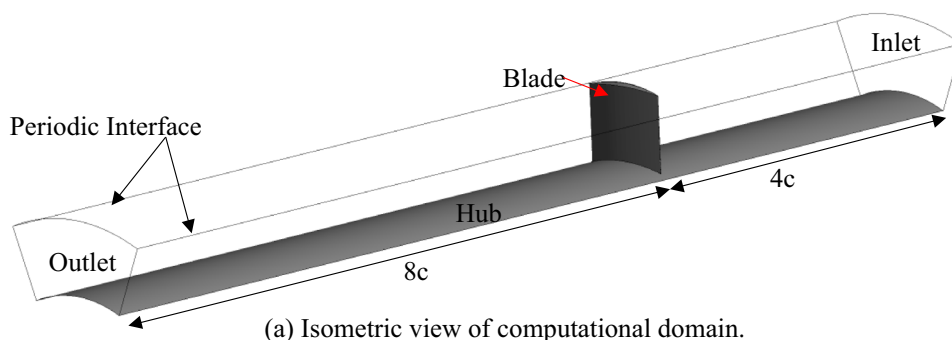
turbine performance and optimize tip flow conditions. Computational studies indicate that tip grooving, a design strategy that achieves a casing groove depth of  $3\%C$ , effectively enhances performance (Torresi et al. 2008; Taha et al. 2011; Halder et al. 2015). The tip leakage flow (TLF) plays a significant role in turbine stall conditions, and mitigation techniques, such as a venturi tube-type duct model, effectively extend the working range (Shaaban and Hafiz 2012). A blade with a radiused tip helps control the secondary flow interaction, blocking the passage vortex. This design modification reduces separation bubbles, prevents internal gap loss, and increases power output by up to 37%. The interaction between TFL and mainstream flow is mitigated using a radiused tip blade, leading to a broader operating range of up to 25%. This design modification is a promising approach for improving turbine performance, backed by various scientific studies (Bindon 1987; Kumar et al. 2021).

Extensive research on Wells turbines aims to improve performance and broaden operational capabilities. Various strategies have been examined, such as blade design alterations, auxiliary turbines, and additional guide vanes. Numerical studies indicate suction slots can postpone stalls,

although with a marginal decrement in second-law efficiency. Stall fences serve to widen the turbines' operational range but modify torque at higher flow coefficients compared to the baseline turbine (Setoguchi et al. 2003b; Okuhara et al. 2013; Shehata et al. 2017a, b; Das and Samad 2020).

Vortex generators (VGs) are commonly used in turbomachinery operations to create vortices in the boundary layer, delaying flow separation. In contrast to lateral vortices, VGs create quasi-steady longitudinal vortices that effectively reduce flow separation (Lin 2002). The secondary flow can be controlled using end wall fences, which induce a streamwise vortex. The height of the fences mainly determines the effectiveness of secondary flow control. The drag effect can be reduced using passive and active boundary layer fences. Both fence types improved the lift coefficient, effectively controlling the cross-flow development (Moon and Koh 2001; Walker and Bons 2018). Streamwise end wall fences prevented the horseshoe vortex moment from transitioning to the suction side, reducing the amalgamation of the low-energy vortex (Govardhan et al. 2006). End wall fence installation, especially the optimal size fence, controlled the flow turning moment by up to 50% and reduced the penetration of the passage vortex. These modifications promise to enhance turbomachinery performance, reducing the likelihood of flow separation (Kumar and Govardhan 2011).

Investigating unique flow control strategies is essential for enhancing wind turbine performance. Zhong et al. (2019) discovered that a leading edge (LE) cylinder on a wind turbine blade increased average tangential force and relative power coefficients by 210.9% and 42.1%, respectively (Zhong et al. 2019). Another study employed the spanwise cylinder wake generated by the vortex to intensify turbulence in the boundary layer and control flow separation (Lin et al. 1990). Further research examined micro-cylinders' efficacy near the LE to suppress separation, suggesting that installing LE-microcylinders could improve turbine performance (Luo et al. 2017; Wang et al. 2018). After installing the leading edge microcylinder (LEM) and the D-cylinder in the Wells turbine, Sadees et al. (2021) observed an 11.11% increase in the operational range. This study includes additional flow analysis and a parametric study of the cylinder's placement in the chordwise direction. In contrast, Geng et al. (2021) optimized the LEM's placement along the spanwise direction. To maintain symmetry, spanwise microcylinders were installed on both the pressure and suction sides of the Wells turbine blade. The results showed a 19.15% enhancement in the relative operating range and a 26.57% increase in peak torque. The accumulated power output improved by 54.2%, and boundary layer instability was reduced by implementing the micro-cylinder (Geng et al. 2023). Sadees et al. (2023) examined the LE-microcylinder (LEM) parameters within the Wells turbine. Their research reveals that a LEM cylinder with a diameter of  $2\%C$  significantly enhances the operating

**Fig. 3** Workflow chart of this study**Fig. 4** Periodic computational domain

range up to 22.22%, mainly when the space between the LEM and the rotor blade ranges from  $2\%C$  to  $3.5\%C$ . Notably, the space lengths of  $2.5\%C$  and  $3.5\%C$  yield a higher torque output (Sadees et al. 2023). These optimal LEM parameters have been employed to further probe the characteristics of prism-surfaced cylinders in the current study. The sharp corners of the prism cylinders (PCs) influence the fluid inflow. This study thoroughly investigates the fluid flow dynamics influenced by these PCs.

This study explores the potential of PCs for enhancing flow separation control in turbines under steady-state

flow conditions. The goal is to manipulate boundary layer flow separation by transferring kinetic energy to the turbine's SS, building on Yang et al. (2018), who found that multi-prism cylinders induce non-fixed, multi-periodic vortex shedding frequencies with high amplitude vibration. Numerical simulations were conducted to assess the impact of installing leading-edge micro-size PCs on a Wells turbine rotor leading-edge. The various cylinder configurations effectively influenced the reduction of boundary layer flow separation and extended the operating range of the Wells turbine. The PCs were installed in the chordwise direction of the

**Table 1** Turbine specifications

No of blades	8
Aerofoil profile	NACA 0015
Chord length	125 mm
Tip radius	300 mm
Mean radius	250 mm
Hub-to-tip ratio	0.67
Solidity	0.64
Clearance	1.25 mm (1% chord length)
Rotation speed	2000 rpm

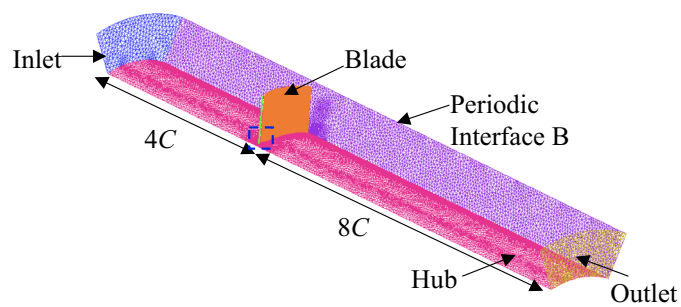
**Table 2** Boundary conditions

Working fluid	Air
Nature of flow	Incompressible
Computational domain	Single blade with a periodic interface
Inlet	Velocity inlet
Outlet	Pressure outlet
Blade, shroud, and hub	No-slip wall
Reference pressure	1 atm
Turbulence intensity	5%
Turbulence model	$k-\omega$ SST
Residual convergence criteria	$1 \times 10^{-5}$

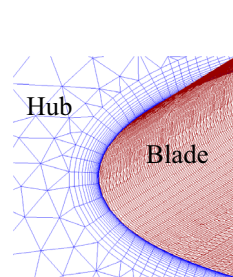
turbine, maintaining its symmetry. This research highlights the beneficial impact of leading-edge PCs on enhancing turbine performance. It implies that using micro-size PCs with sharp edges to manage the separated flow could offer a viable basis for efficient and sustainable wave power generation and deserves further examination.

This paper is divided into four sections. Section 1 presents an introduction and literature review of the study. Section 2 provides information about the computational domain and mesh generation. Section 3 includes a grid sensitivity study,

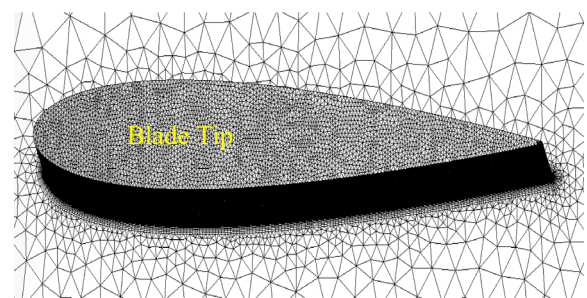
**Fig. 5** Mesh configurations of computational domain



(a) Isometric view

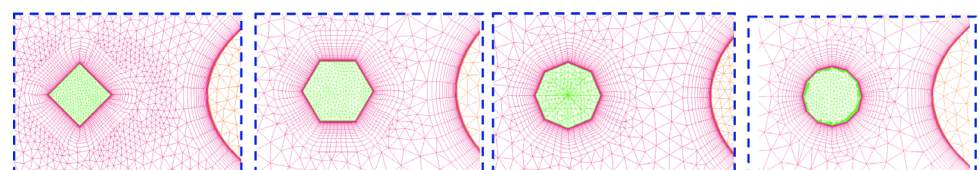


Mesh close to hub



Mesh at the tip

(b) Prism layers in the reference blade LE and mesh at the tip.



(i) SC

(ii) HC

(iii) OC

(iv) DC

(c) Prism layers close to cylinder and blade LE.



**Table 3** Grid uncertainty analysis

Number of elements ( $10^6$ )	$N_1, N_2, N_3$	7.79, 3.53, 1.61
Average grid size ( $h$ )	$h_1, h_2, h_3$	0.005043, 0.006564, 0.008536
Grid refinement factor ( $r$ )	$r_{21}, r_{32}$	1.3, 1.3
Critical parameter studied ( $\phi$ )	$\phi_1, \phi_2, \phi_3$	0.135064, 0.133836, 0.126194
Apparent order	$P$	6.8
Extrapolated values	$\phi_{ext}^{12}, \phi_{ext}^{32}$	0.135342, 0.135352
Approximation relative error (%)	$e_a^{21}, e_a^{32}$	0.93%, 5.71%
Extrapolated relative error (%)	$e_{ext}^{21}, e_{ext}^{32}$	0.18%, 1.12%
Grid convergence index (%)	$GCI_{fine}^{21}, GCI_{medium}^{32}$	0.23%, 1.42%

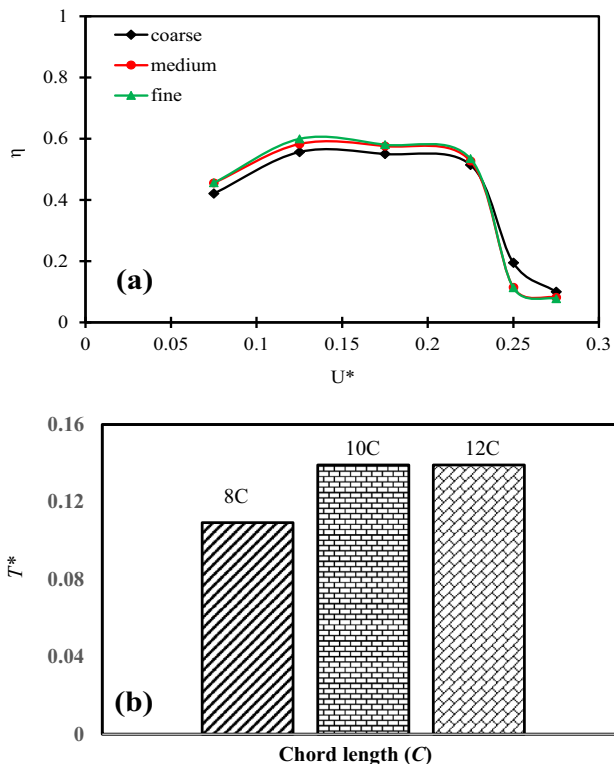


**Fig. 6** a Grid independency study. b Domain independent study

numerical validation using existing experimental and numerical studies, and a comprehensive flow field analysis. Lastly, Sect. 4 provides a conclusive summary of this study.

## 2 Computational domain

A CAD model was employed to create a turbine blade’s computational domain based on the Torresi et al. (2008) design. The diagram presented in Fig. 3 illustrates the workflow of the ongoing study, providing a step-by-step depiction of the approach utilized. The periodic domain features eight blades with a NACA0015 profile and  $C = 0.125$  m, as depicted in Fig. 4. The rotor blade profile has a solidity of 0.644 m,

‘ $R_{hub}$ ’ and ‘ $R_{tip}$ ’ values of 0.2 m and 0.3 m, respectively, and a hub-to-tip ratio of 0.67. A clearance gap of 1% $C$  is maintained between the shroud and tip. The computational domain lengths were set at 4 $C$  upstream and 8 $C$  downstream (Setoguchi et al. 2003a; Hashem et al. 2018). The simulation used a single blade, with periodic interface boundary conditions enforced circumferentially. Additional information on the computational flow domain can be found in Table 1 (Torresi et al. 2008).

Enhancing grid resolution and including sufficient nodes close to the wall boundary is necessary to simulate fluid movement in the boundary layer. Employing ANSYS CFX’s SST  $k-\omega$  model accounts for shear caused by viscosity in the near-wall region. An automatic wall function maintains a minimum non-dimensional wall distance ( $y^+ < 1$ ) for the SST  $k-\omega$  model to balance computational efficiency with accuracy. For optimal performance of the automatic wall function in CFX’s SST  $k-\omega$  model,  $y^+$  values should remain below 1 (ANSYS-CFX 2011; Halder et al. 2015; Das and Samad 2020).

The accurate definition of flow simulation and reliable results heavily rely on appropriate boundary conditions. Selecting proper boundary conditions is crucial in representing the physical situation of the problem being studied (ANSYS-CFX 2011). The numerical simulation implemented boundary conditions at the velocity inlet and pressure outlet. The hub, shroud, and blade surfaces acted as solid walls, while periodic boundary conditions were applied tangentially to simulate the repeating geometry of the turbine. These boundary conditions enabled us to simulate the complex nature of fluid flow conditions. The careful selection of boundary conditions is necessary for accurate flow simulations in complex geometries. Table 2 describes the boundary conditions in detail. Figure 5 depicts the discretized computational flow domain with the number of grids. This illustration represents the prism layers developed close to the blade’s cylinders and hub section. An optimal grid configuration enables precise numerical simulations for fluid dynamics

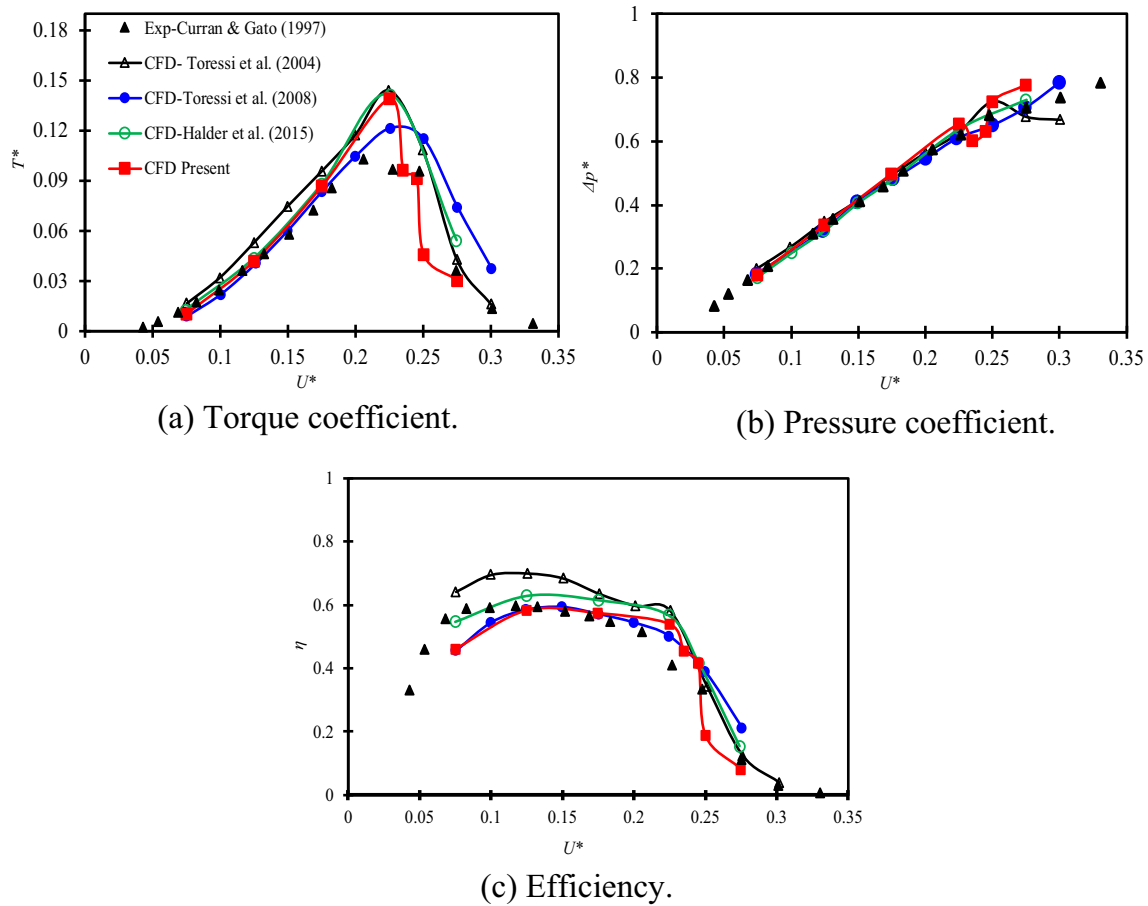


**Fig. 7** Performance validation of experimental and computational study

analysis. The supercomputing facility at IIT Madras, Chennai, was used to conduct numerical simulations, with each case taking 8–10 h to complete.

### 3 Results and discussion

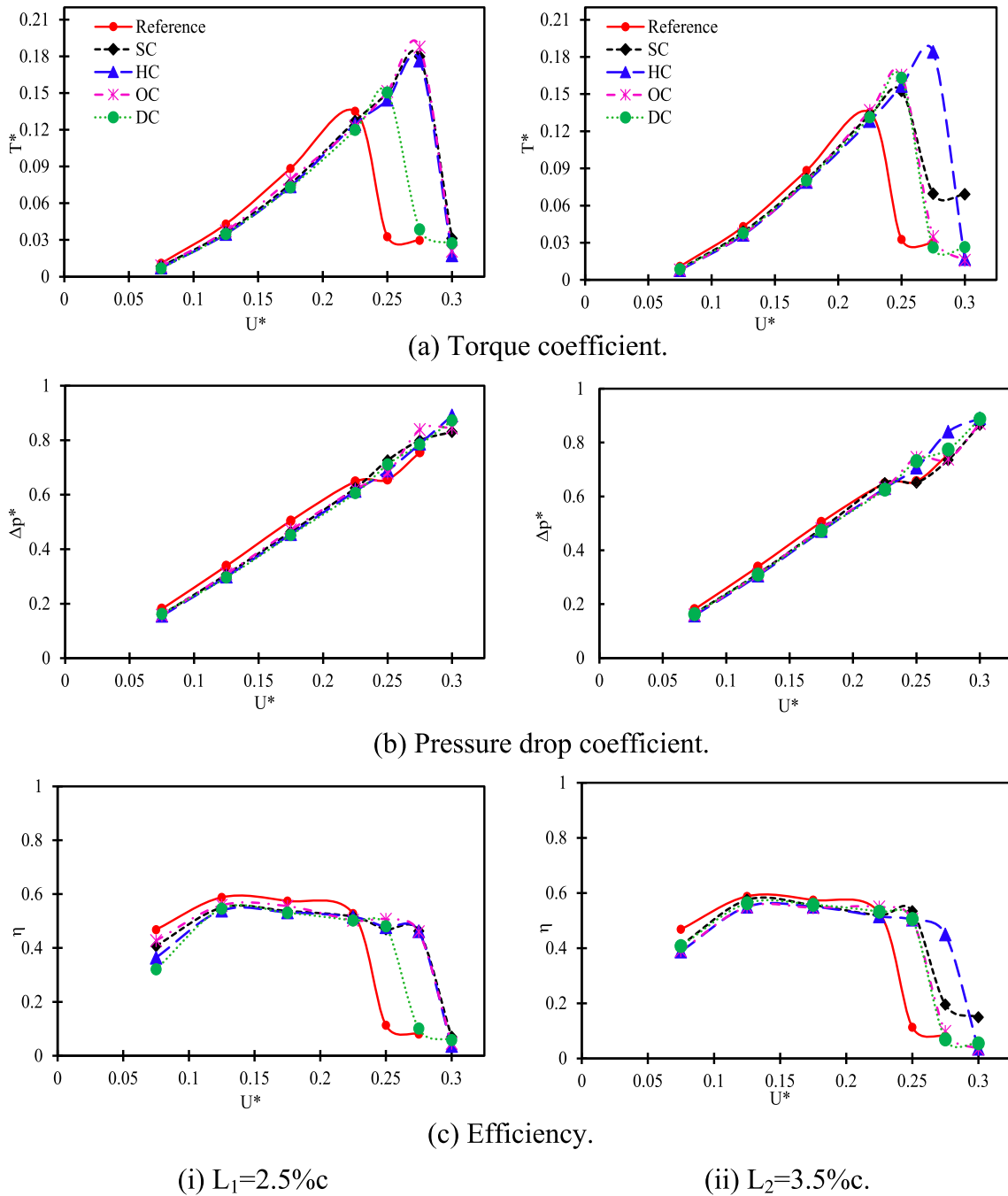
#### 3.1 Grid sensitivity study

Table 3 displays the outcomes of an uncertainty analysis conducted on the reference turbine's computational grids. GCI was assessed for three grid sizes: coarse (1.61 M), medium (3.53 M), and fine (7.79 M). A consistent grid growth ratio maintained uniform mesh refinement across all refined grids. Celik et al. (2008) suggested using a refinement factor 1.3 and selecting the torque coefficient as the critical performance parameter (Celik et al. 2008). As grid resolution increases, GCI decreases, with GCI values of 0.23% and 1.42% for the fine and medium grids, respectively. The acquired GCI fell below the acceptable 2% threshold, confirming spatial grid convergence on the medium-sized grid (Manna et al.

2013). The medium-sized grid was selected for subsequent analysis, and Fig. 5 illustrates the discretized flow domain containing the optimal grid quantity and Fig. 6a shows the grid convergence study of the entire flow coefficient ( $U^* = 0.075$ – $0.275$ ). Based on domain sensitivity analysis, the downstream domain length is four times the chord length, while the upstream domain length is eight times the chord length, and Fig. 6b depicts it.

#### 3.2 Computational validation

The proposed computational model was compared with existing CFD and experimental data from the literature to ensure its accuracy. The comparison was made against the results reported by Curran and Gato (1997), numerical results by Toressi et al. (2004, 2008), and Halder et al. (2015), as presented in Fig. 7. Plotting stagnation pressure drop coefficient ( $\Delta P^*$ ), torque coefficient ( $T^*$ ), and efficiency ( $\eta$ ) was done for various flow coefficients. The computational results generally agree well with the experimental data, particularly for the pressure drop coefficient, until the stall point was reached



**Fig. 8** Performance of prism rod assisted Wells turbine

in Fig. 7b. However, agreement with the experimental results for torque coefficient was also observed before the stall point was reached in Fig. 7a. The effect of frictional forces on the rotating portion of the hub was considered, and the pressure and shear stress terms on the blade surface were used to compute the results (Torresi et al. 2008). To retain accuracy, the discretization method for the tip gap region and secondary flow was related to the experimental data of Curran and Gato (1997). The deviations in the computational and

experimental data were minimal, with the pressure, torque, and efficiency coefficients observing  $\pm 0.4\%$ ,  $\pm 3.55\%$ , and  $\pm 1.5\%$  differences, respectively.

### 3.3 Analysis of the flow characteristics

This section examines the impact of prism cylinder (PC) location and shapes on flow separation in Wells turbines, specifically analyzing the flow characteristics. Eight test



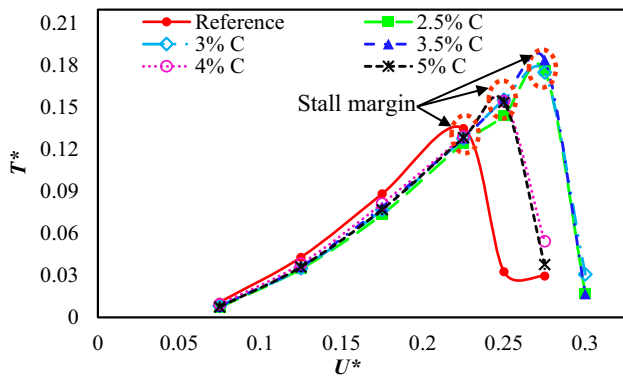


Fig. 9  $T^*$  value of various gap between hexagonal PC to rotor LE

cases were conducted, each utilizing a PCs with equivalent circumferential length but varying shapes. The resulting data was abbreviated as SC (square cylinder), HC (hexagonal cylinder), OC (octagonal cylinder), and DC (decagonal cylinder) for ease of reference, as presented in Fig. 8. Additionally, Fig. 5 provides further insight into the formation of the prism layer in the cylinder-rotor configuration. While the circumferential length of each PCs remained constant at  $2\%C$ , the face length and internal angle were varied. The analysis also incorporated two different space lengths ( $L_1 = 2.5\%C$  and  $L_2 = 3.5\%C$ ) between the PCs and the LE of the rotor blade for different prism cylinders (square, hexagonal, octagonal, and decagonal).

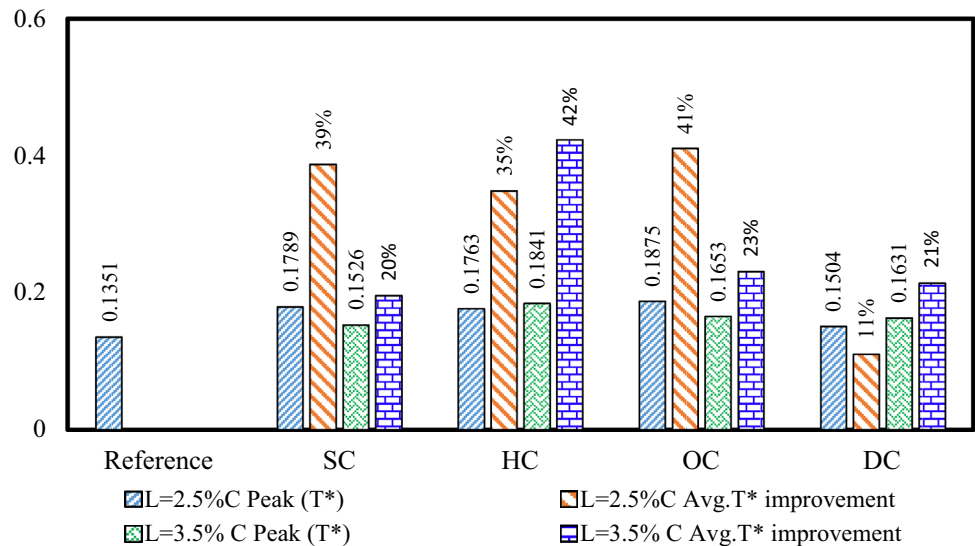
The performance parameter graphs in Fig. 8 reveal a significant increase in the torque coefficient value of the prism cylinder-assisted Wells turbine (PCAWT) compared to the baseline turbine, with an improved operating range from 11.11 to 22.22%. However, the overall efficiency of the PCAWT system decreased due to obstruction in the incoming flow, leading to dissipation loss. The analysis further

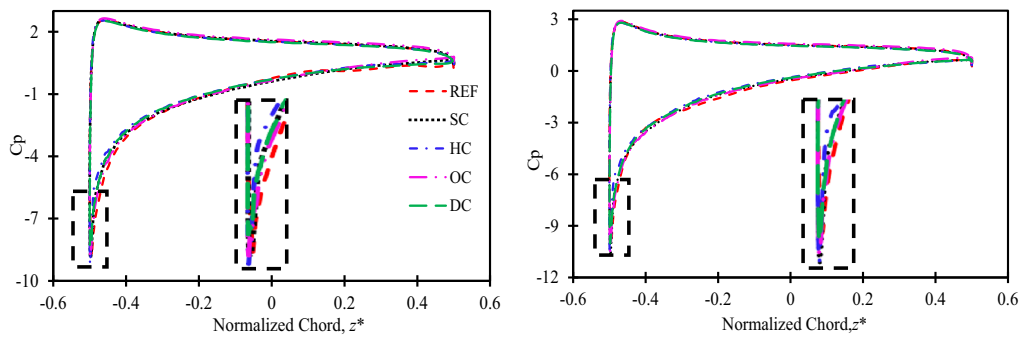
examined the hexagonal prism cylinder (HC) for both space length cases ( $L_1 = 2.5\%C$  and  $L_2 = 3.5\%C$ ), which provided a higher operating range of 22.22% in both modified cases. The hexagonal prism cylinder (PC) has demonstrated superior performance to other PC configurations. This study seeks to identify the optimal gap between the PC and the rotor leading edge (LE) through an extended gap analysis of the hexagonal-PCAWT. The performance curve ( $T^*$ ), presented in Fig. 9, indicates an improvement in the operating range of up to 22.22% at gaps of 2.5% $C$ , 3% $C$ , and 3.5% $C$ . Notably, the maximum peak torque is observed at the 3.5% $C$  gap, and the peak torque value is similar in both 2.5% $C$  and 3% $C$ . On the other hand, in the 4% $C$  and 5% $C$  gaps, the stall margin shifts only up to 11.11%.

Figure 10 displays the various PCAWT peak and average  $T^*$  values, showing an improvement in  $T^*$  value from a minimum of 11% (DC- in  $L_1 = 2.5\%C$ ) to a maximum of 42% (HC- in  $L_2 = 3.5\%C$ ). The HC-assisted Wells turbine demonstrated a better operating range (22.22%) and  $T^*$  value in both space lengths ( $L_1 = 2.5\%C$  and  $L_2 = 3.5\%C$ ).

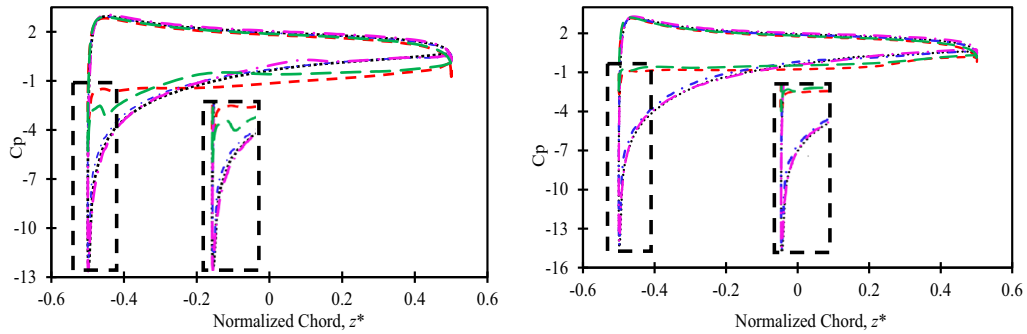
Figure 11a, b illustrates the blade loading curve at mid-span and 95% span lengths (close to the tip), featuring two distinct  $U^*$  values. The flow coefficient impacts the baseline turbine and the modified PCAWT similarly, with minor differences evident in the area of the pressure and suction sides at  $U^* = 0.225$ . Reducing the space between the curves decreases the performance of both turbines. However, beyond a certain point, flow separation occurs, known as a stall point or critical stalling, which is delayed in PCAWT compared to the baseline model. The blade loading curve’s pressure distribution between the pressure and suction sides provides detailed information on post-stall conditions. The vortex generated by PCAWT has higher momentum and kinetic energy than the normal flow on the SS of the baseline

Fig. 10 Peak and average  $T^*$  improvement on PCAWT on  $L = 2.5\%C$  and  $3.5\%C$





(a)  $U^*=0.225$ .

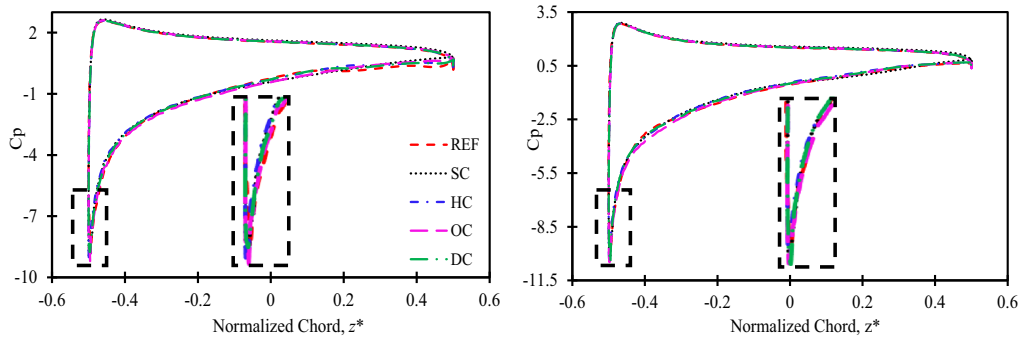


(b)  $U^*=0.275$ .

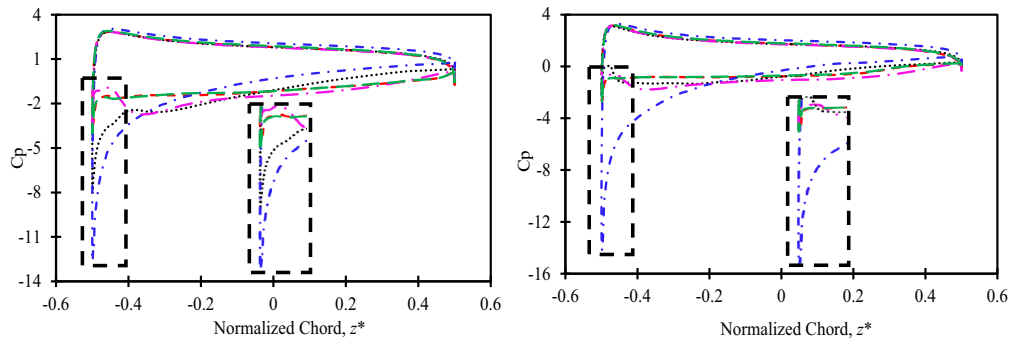
(i) *Mid span.*

(a)

(ii) *Tip.*



(a)  $U^*=0.225$ .



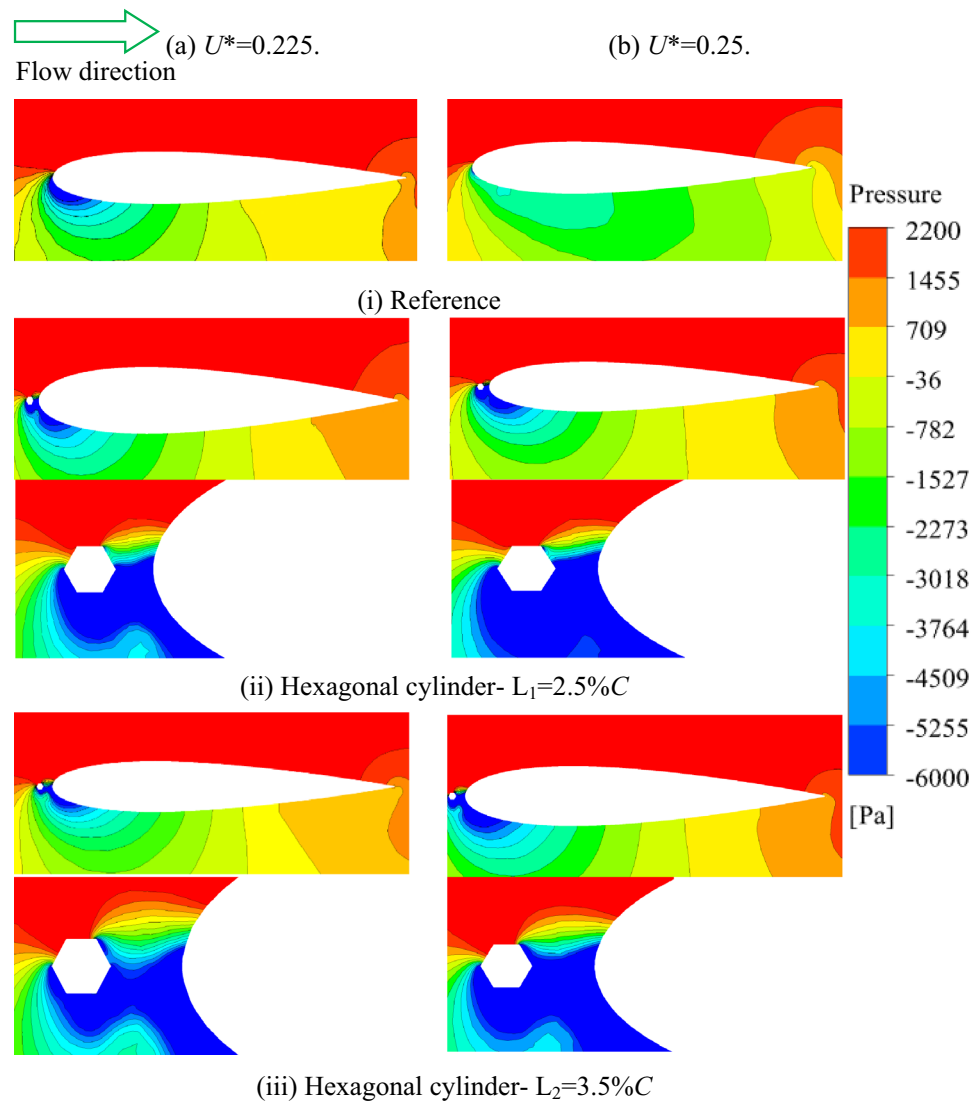
(b)  $U^*=0.275$ .

(i) *Mid span.*

(b)

(ii) *Tip.*

**Fig. 11** **a** Pressure distribution on two span lengths of  $L_1 = 2.5\%C$  (i) mid span, (ii) tip. **b** Pressure distribution on two span lengths of  $L_2 = 3.5\%C$  (i) mid span, (ii) tip

**Fig. 12** Pressure contour on mid span

turbine, transferring momentum to the separated boundary layer flow and energizing it. At  $U^* = 0.275$  in  $L_1 = 2.5\%C$  for (SC, HC, and OC), flow attachment is maintained in PCAWT, whereas in DC-PCAWT, a stall occurs at  $U^* = 0.250$ . Moreover, HC-PCAWT demonstrated a marked improvement at  $L_2 = 3.5\%C$ , with a stall captured at  $U^* = 0.250$  for the SC, OC, and DC-PCAWT, whereas the modified turbine design.

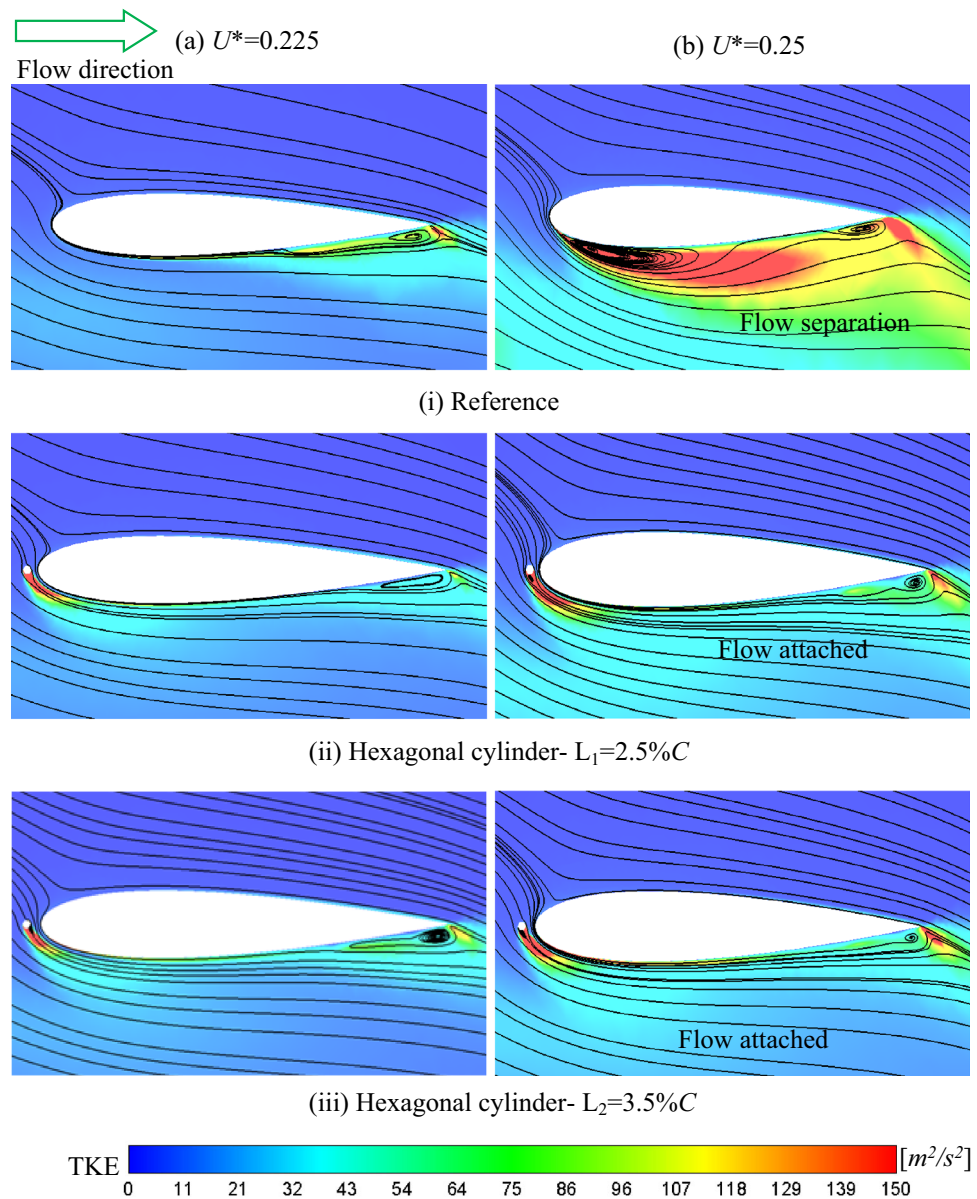
Figure 12 displays the pressure contours for HC-PCAWT and baseline cases across two  $U^*$  (0.225 and 0.25) values at the blade mid-span. At  $U^* = 0.225$ , both models demonstrate smooth flow attachment to the suction surface (SS). A closer look at PCAWT in Fig. 12 reveals pressure variations on either side of the PC surface. The flow separation is observed from the SS due to the adverse pressure gradient effect at higher  $U^*$  values in the baseline case. However, the PCAWT's flow remains attached and extends the turbine's operating range due to the vortex generated by the PC that

transfers kinetic energy to separate flow in the SS of the rotor at  $U^* = 0.25$ .

Figure 13 depicts the streamlines and turbulent kinetic energy (TKE) contour, revealing that at the flow coefficient at the stall point ( $U^* = 0.225$ ), both the baseline and modified models have closely attached streamlines to the SS. However, at a higher  $U^*$  value ( $U^* = 0.25$ ), the modified PCAWT, utilizing the PC's ability to manipulate the separated flow at the SS, demonstrates significantly improved boundary layer flow attachment compared to the baseline model, which has separated flow from the SS. The base model leads to a recirculation zone formation in the SS. Furthermore, the lower TKE value observed in the modified PCAWT compared to the baseline model indicates improved flow attachment and blade loading (see Fig. 11).

Streamlines offer a visual display of flow attachment to the SS. Figure 14 showcases the baseline and modified cases' SS streamlines. The blade SS flow maintains smooth attachment

**Fig. 13** Turbulent kinetic energy contour with streamlines on mid span



at a flow coefficient ( $U^* = 0.225$ ). Nevertheless, there is a flow separation at a flow coefficient value ( $U^* = 0.25$ ) after stalling in the baseline model, causing the baseline turbine flow to detach from the SS. However, in the PCAWT, flow separation is avoided, and attachment to the blade SS is maintained despite a higher flow coefficient ( $U^* = 0.25$ ). This effect increases PC-Well turbine torque output, in agreement with Fig. 7 findings depicting the PCAWT effect on hexagonal prism cylinder cases.

Figure 15 presents the pressure coefficient ( $C_p$ ) contour for the baseline and HC-PCAWT models at blade SS and pressure surface (PS) for two different  $U^*$  values. At a lower  $U^*$  value, even flow attachment was observed throughout the SS in both models, with enhanced  $C_p$  distribution in the

PCAWT model SS at  $U^* = 0.225$ . The  $C_p$  distribution in the PS exhibited similar effects in both models. At higher  $U^*$  values, the baseline model suffered from the stall effect, causing flow separation from the SS due to the adverse pressure gradient effect. However, the PCAWT model with the PC substantially improved the  $C_p$  distribution on the SS compared to the baseline model. At  $U^* = 0.25$ , the PCAWT model demonstrated an attached flow and extended to the operating range up to 22.22%. Here, a leading-edge PC generated a vortex that transferred the kinetic energy to the separated flow and prevented the SS flow separation.

Figure 16 illustrates the non-dimensional distribution of tangential velocity along the spanwise direction in proximity to the leading edge of the rotor blade. The tangential velocity

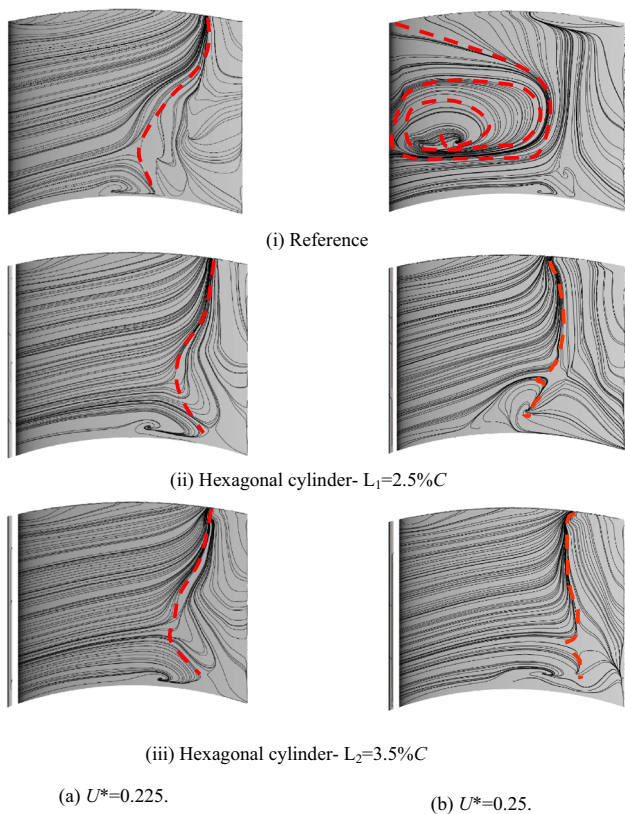


Fig. 14 Streamline distribution on SS

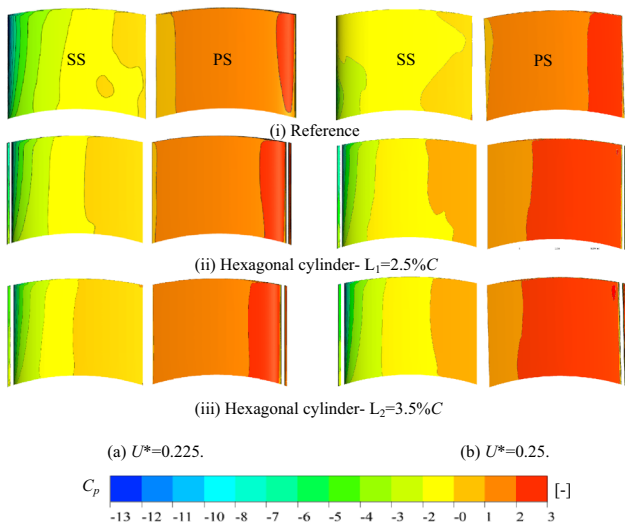


Fig. 15  $C_p$ -distribution along SS and PS

directly influences the torque generated by the turbine rotor. A higher tangential velocity corresponds to increased torque production from the turbine rotor, aligning with the observations in Fig. 8a. At a lower  $U^* = 0.225$ , representing the stall margin of the reference Wells turbine, there is a marginally higher tangential velocity than the hexagonal-PCAWT rotor.

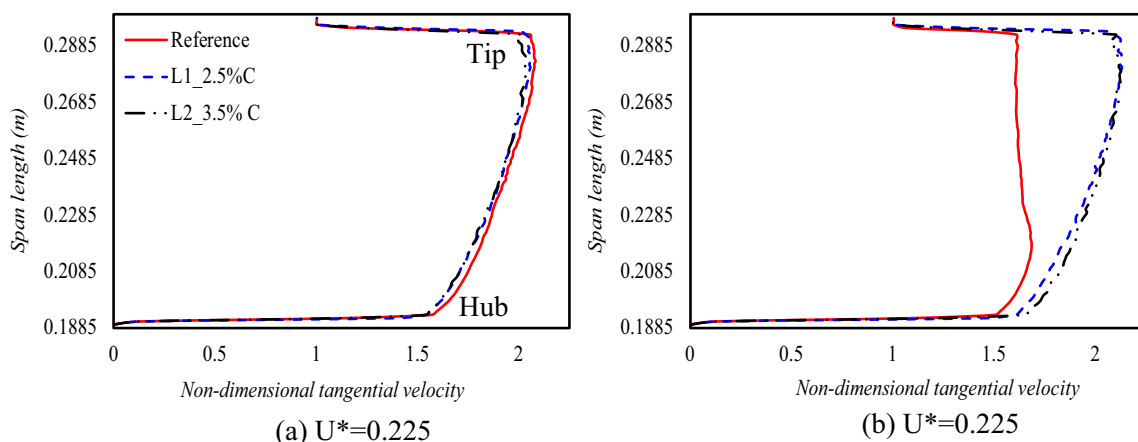
Conversely, at the post-stall point of  $U^* = 0.25$ , the tangential velocity of the reference turbine is considerably lower than that of the hexagonal-PCAWT (with  $L_1 = 2.5\%C$  and  $L_2 = 3.5\%C$ ). This indicates a sudden decline in torque output for the reference turbine due to stall occurrence.

Figure 17 shows the tangential velocity distribution contour at three different planes in the chordwise direction of the rotor blade. At lower  $U^*$  values of 0.225, the baseline and PCAWT cases exhibited similar effects, consistent with the findings in Figs. 7, 8, 9, 10 and 11. However, at higher  $U^*$  values (or post-stall condition) of 0.25, the baseline turbine experienced flow separation from planes 1 to 3, whereas the PCAWT cases maintained smooth flow attachment to all three planes. The HC introduced incoming fluid and generated vortices that transferred kinetic energy to the separated flow, improving the boundary layer flow conditions and increasing the operating range of the PCAWT by 22.22%. The PCAWT demonstrated superior results to the baseline turbine model due to the manipulation of boundary layer flow using the hexagonal prism cylinder, which prevented flow separation at higher  $U^*$  and allowed the turbine to perform efficiently over a broader range of operating conditions.

The  $z$ -vorticity contour and volume streamlines are presented at a mid-chord section in Fig. 18. For  $U^* = 0.225$  and below, the volume streamlines remain smoothly attached. However, at higher  $U^* = 0.25$ , the mainstream flow interacts strongly with the secondary flow, causing detachment from the SS (as seen in Fig. 18 for the baseline model). In contrast, the PCAWT model demonstrates reduced interaction, which improves attachment length and subsequent torque output (as illustrated in Fig. 8).

In discussing the tip leakage flow, the focus is primarily on dealing with leakage flow in the tip of the rotor blade. Figure 19 depicts the  $C_p$  distribution, and the tip leakage flows through volume streamlines. The tip leakage vortex (TLV) formation begins downstream and propagates to the upstream side. The scale of the vortex formation varies according to the angle of attack (AoA), with increasing AoA leading to an increase in the scale value of the vortex. At a flow coefficient ( $U^* = 0.225$ ), the tip leakage flow generates a lower TLV, as evidenced in Fig. 19. Conversely, increasing the  $U^*$  value to 0.25 strengthens the TLV in the baseline model. However, the PCAWT experiences reduced TLV at both  $U^*$  values; the premature flow separation has been controlled due to this effect.





**Fig. 16** Non-dimensional tangential velocity distribution near blade LE

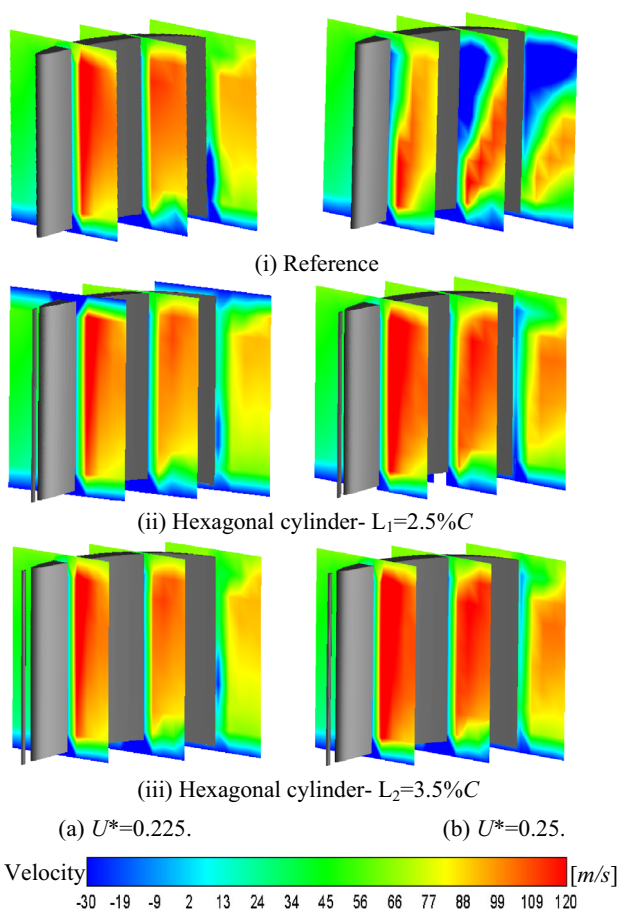


**Fig. 17** Tangential velocity contour different chordwise plane

## 4 Conclusions

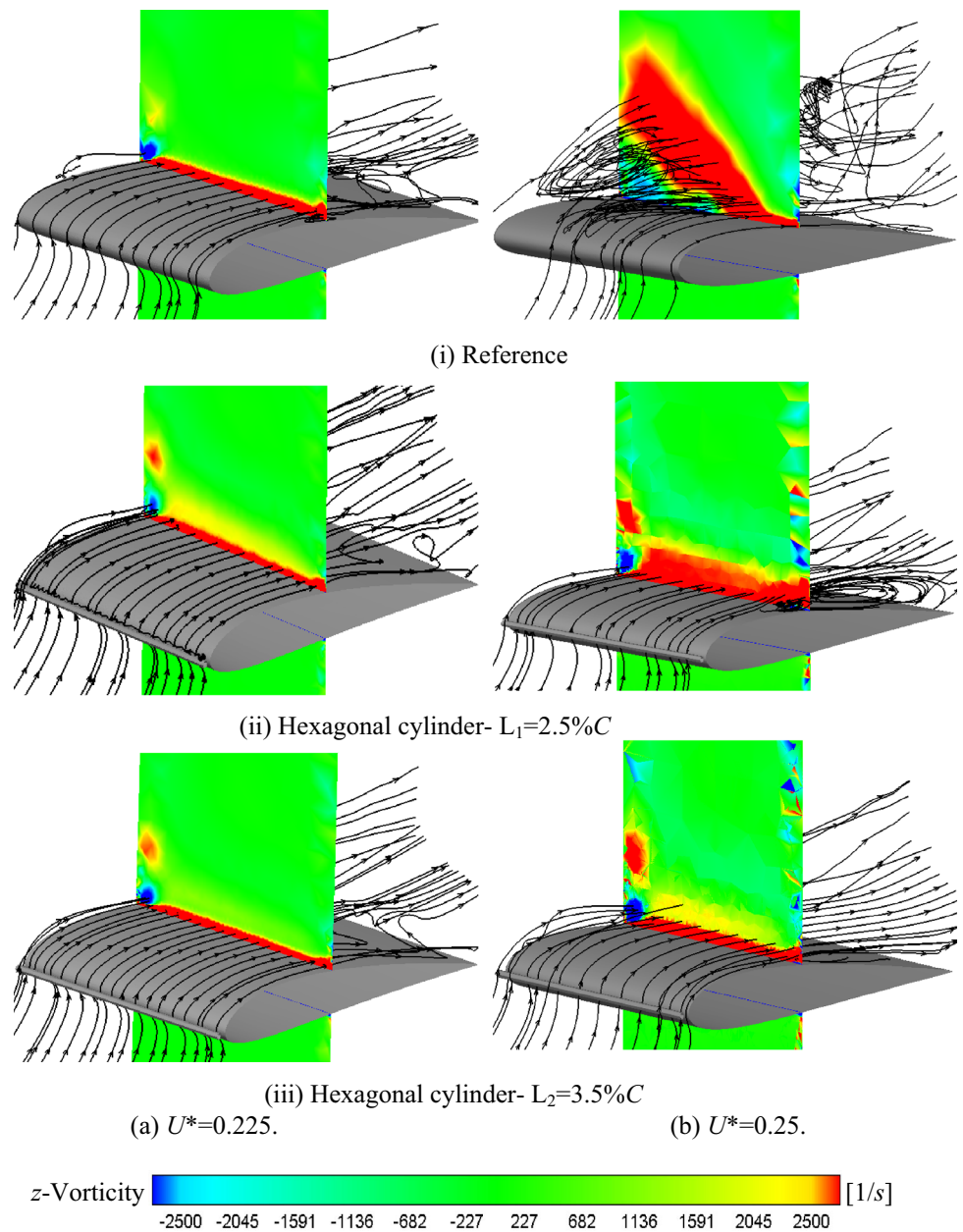
In summary, this investigation explored the effectiveness of using prism cylinders (PCs) to influence the boundary layer and ultimately enhance the performance of the Wells turbine. The analysis of results, which included tangential velocity

distribution, pressure coefficient distribution,  $z$ -vorticity contour, volume streamlines, and tip leakage flow, showed that the PCAWT outperformed the baseline model primarily by reducing flow separation from the blade SS. The PCAWT also demonstrated an increased operating range of up to 22.22% and reduced TLV formation. The PCs facilitate transmitting the kinetic energy into the SS of the blade, leading to higher torque output. The study's outcomes can be used to upgrade the turbine's performance in future uses.

The following are essential findings from this study:

- The presence of PC significantly increases the Wells turbine's operating range by effectively controlling flow separation. By reenergizing the separated flow in the SS, the PC facilitates reattachment and shifts the maximum stall point from a flow coefficient of 0.225–0.275.
- The formation of counter-rotating vortices plays a crucial role in this process by facilitating momentum transfer to a separated flow, leading to delays in the flow separation.
- Considerations for the gap between the PC and rotor blade, as well as the circumference of the PC, are essential. The study found that peak torque coefficient values were improved at HC-PCAWT in  $L_2 = 3.5\%C$  with  $U^* = 0.275$ , resulting in a 42% increase compared to the reference case.
- On average, the peak torque showed a 42.28% improvement, while a moderate decrease in efficiency of 5.28% was observed due to dissipation loss.

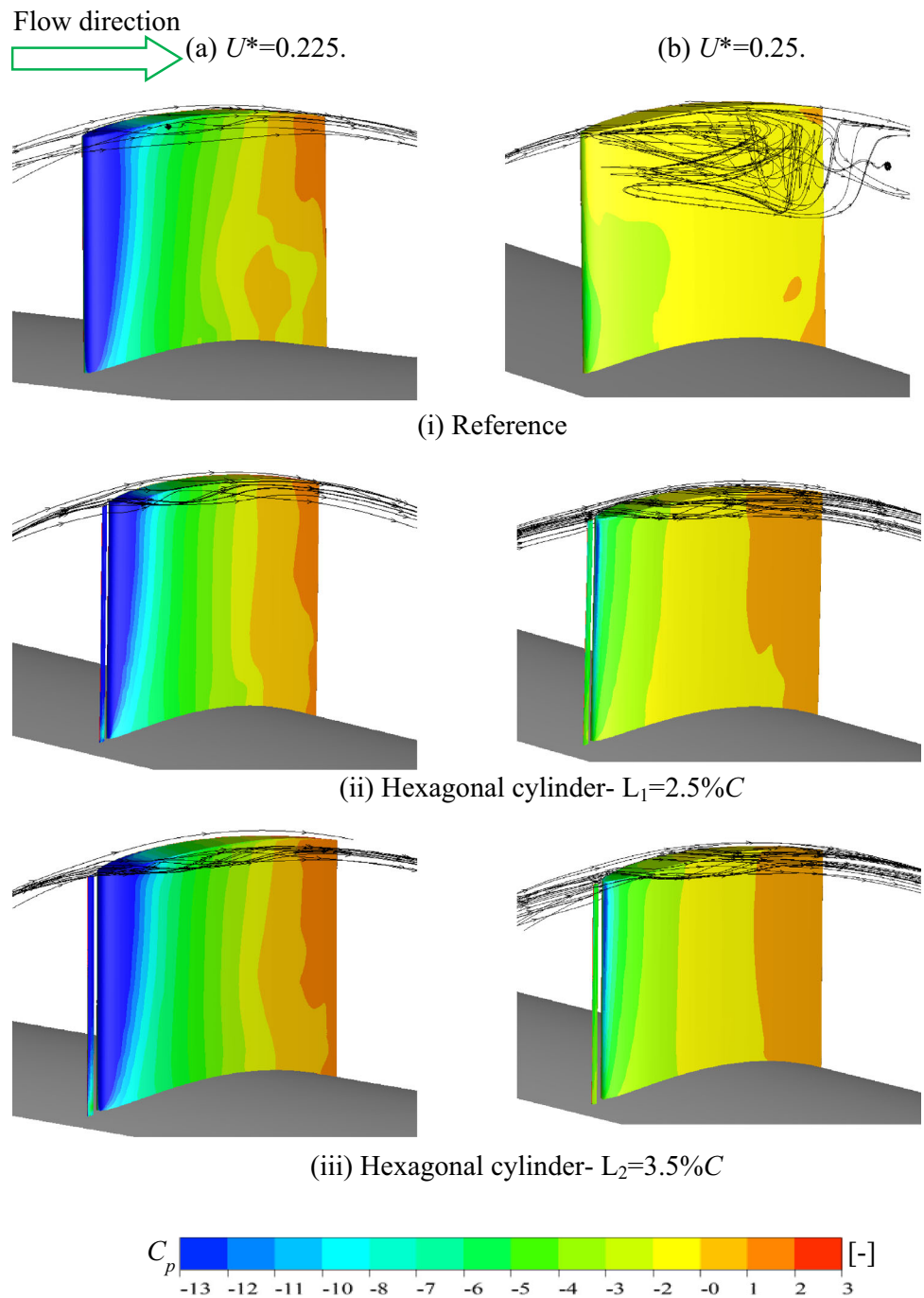
**Fig. 18**  $z$ -vorticity contour along with volume streamlines on mid-chord



The current study expands on previous research concerning circular shape leading-edge microcylinders (LEM) and is centered explicitly on parametric optimization. However, future work is planned to carry out a multi-objective optimization of the prism cylinders (PCs) parameters,

encompassing circumferential length, internal angle of the prism, gap between the leading edge to PCs, and orientation. This forthcoming research endeavors to create a high-performance Wells turbine with amplified torque and operating range.

**Fig. 19**  $C_p$ -distribution along with tip leakage vortex



**Acknowledgements** The authors are grateful to the Indian Institute of Technology Madras (IIT Madras) in Chennai, Tamil Nadu, for providing the facilities and support that made this research possible.

**Author contributions** PS conceptualization, methodology, software usage, validation, formal analysis, investigation, data curation, writing—original draft, visualization. AS resources, writing—review and editing, supervision.

**Data availability** The data will be provide on request.

## Declarations

**Conflict of interest** The authors solemnly affirm that their work in this paper remains free from any financial affiliations or personal relationships that could have influenced its content. This extends to any potential conflicts of interest involving organizations or individuals who might stand to gain from the outcomes of this study. We emphasize our unwavering dedication to upholding scientific integrity and fostering transparency in every aspect of our research endeavors.

## References

- Amundarain M, Alberdi M, Garrido AJ et al (2010) Wave energy plants: control strategies for avoiding the stalling behaviour in the Wells turbine. *Renew Energy* 35:2639–2648. <https://doi.org/10.1016/j.renene.2010.04.009>
- ANSYS-CFX (2011) ANSYS CFX-solver modeling guide
- Badhushah R, Samad A (2015) Multiple surrogate based optimization of a bidirectional impulse turbine for wave energy conversion. *Renew Energy* 74:749–760. <https://doi.org/10.1016/j.renene.2014.09.001>
- Barstow S, Mørk G, Mollison D, Cruz J (2007) The wave energy resource. *Ocean Wave Energy*. [https://doi.org/10.1007/978-3-540-74895-3\\_4](https://doi.org/10.1007/978-3-540-74895-3_4)
- Bindon JP (1987) Pressure distributions in the tip clearance region of an unshrouded axial turbine as affecting the problem of tip burnout. In: *Proc ASME Turbo Expo 1*. <https://doi.org/10.1115/87-GT-230>
- Ceballos S, Rea J, Robles E et al (2015) Control strategies for combining local energy storage with wells turbine oscillating water column devices. *Renew Energy* 83:1097–1109. <https://doi.org/10.1016/j.renene.2015.05.030>
- Celik IB, Ghia U, Roache PJ et al (2008) Procedure for estimation and reporting of uncertainty due to discretization in CFD applications. *J Fluids Eng Trans ASME* 130:0780011–0780014. <https://doi.org/10.1115/1.2960953>
- Curran R, Gato LMC (1997) The energy conversion performance of several types of wells turbine designs. *Proc Inst Mech Eng Part A J Power Energy* 211:133–145. <https://doi.org/10.1243/0957650971537051>
- Das TK, Samad A (2020) Influence of stall fences on the performance of wells turbine. *Energy* 194:116864. <https://doi.org/10.1016/j.energy.2019.116864>
- Falcao A (2010) Wave energy utilization: a review of the technologies. *Renew Sustain Energy Rev* 14:899–918. <https://doi.org/10.1016/j.rser.2009.11.003>
- Falcão AFO, Henriques JCC (2016) Oscillating-water-column wave energy converters and air turbines: a review. *Renew Energy* 85:1391–1424. <https://doi.org/10.1016/j.renene.2015.07.086>
- Gato LMC, Warfield V, Thakker A (1996) Performance of a high-solidity wells turbine for an OWC wave power plant. *J Energy Resour Technol* 118:263–268. <https://doi.org/10.1115/1.2793872>
- Geng K, Yang C, Hu C et al (2021) Performance investigation of Wells turbine for wave energy conversion with stall cylinders. *Ocean Eng* 241:110052. <https://doi.org/10.1016/j.oceaneng.2021.110052>
- Geng K, Yang C, Zhao B et al (2023) Residual circulation budget analysis in a wells turbine with leading-edge micro-cylinders. *Renew Energy* 216:119049. <https://doi.org/10.1016/j.renene.2023.119049>
- Gomes RPF, Henriques JCC, Gato LMC, Falcão AFO (2012) Multi-point aerodynamic optimization of the rotor blade sections of an axial-flow impulse air turbine for wave energy conversion. *Energy* 45:570–580. <https://doi.org/10.1016/j.energy.2012.07.042>
- Govardhan M, Rajender A, Umang JP (2006) Effect of streamwise fences on secondary flows and losses in a two-dimensional turbine rotor cascade. *J Therm Sci* 15:296–305. <https://doi.org/10.1007/s11630-006-0296-2>
- Gratton T, Ghisu T, Parks G et al (2018) Optimization of blade profiles for the wells turbine. *Ocean Eng* 169:202–214. <https://doi.org/10.1016/j.oceaneng.2018.08.066>
- Greenblatt D, Pfeiffermann O, Keisar D, Göksel B (2021) Wells turbine stall control using plasma actuators. *AIAA J* 59:765–772. <https://doi.org/10.2514/1.J060278>
- Halder P, Samad A, Kim JH, Choi YS (2015) High performance ocean energy harvesting turbine design—a new casing treatment scheme. *Energy* 86:219–231. <https://doi.org/10.1016/j.energy.2015.03.131>
- Halder P, Samad A, Thévenin D (2017) Improved design of a Wells turbine for higher operating range. *Renew Energy* 106:122–134. <https://doi.org/10.1016/j.renene.2017.01.012>
- Halder P, Mohamed MH, Samad A (2018) Wave energy conversion: design and shape optimization. *Ocean Eng* 150:337–351. <https://doi.org/10.1016/j.oceaneng.2017.12.072>
- Hashem I, Abdel Hameed HS, Mohamed MH (2018) An axial turbine in an innovative oscillating water column (OWC) device for sea-wave energy conversion. *Ocean Eng* 164:536–562. <https://doi.org/10.1016/j.oceaneng.2018.06.067>
- Hyun B, Moon JS (2004) Practical numerical analysis of impulse turbine for OWC-type wave energy conversion using a commercial CFD code. In: *Proc Fourteenth Int Offshore Polar Eng Conf m*:880653
- Inoue M, Kaneko K, Setoguchi T (1985) Studies on wells turbine wave power generator (part 3: effect of guide vanes). *Bull JSME* 28:1986–1991
- Kumar KN, Govardhan M (2011) Secondary flow loss reduction in a turbine cascade with a linearly varied height streamwise endwall fence. *Int J Rotating Mach* 2011:1–16. <https://doi.org/10.1155/2011/352819>
- Kumar PM, Halder P, Samad A (2021) Radiused edge blade tip for a wider operating range in wells turbine. *Arab J Sci Eng* 46:2663–2676. <https://doi.org/10.1007/s13369-020-05185-z>
- Lekube J, Garrido AJ, Garrido I et al (2018) Flow control in wells turbines for harnessing maximum wave power. *Sensors (switzerland)*. <https://doi.org/10.3390/s18020535>
- Lin JC (2002) Review of research on low-profile vortex generators to control boundary-layer separation. *Prog Aerosp Sci* 38:389–420. [https://doi.org/10.1016/S0376-0421\(02\)00010-6](https://doi.org/10.1016/S0376-0421(02)00010-6)
- Lin J, Howard F, Bushnell D, Selby G (1990) Investigation of several passive and active methods for turbulent flow separation control. In: *21st fluid dynamics, plasma dynamics and lasers conference*. American Institute of Aeronautics and Astronautics, Reston, pp 1–21
- Liu Z, Cui Y, Kim KW, Shi HD (2016) Numerical study on a modified impulse turbine for OWC wave energy conversion. *Ocean Eng* 111:533–542. <https://doi.org/10.1016/j.oceaneng.2015.11.005>
- López I, Pereiras B, Castro F, Iglesias G (2016) Holistic performance analysis and turbine-induced damping for an OWC wave energy converter. *Renew Energy* 85:1155–1163. <https://doi.org/10.1016/j.renene.2015.07.075>
- Luo D, Huang D, Sun X (2017) Passive flow control of a stalled airfoil using a microcylinder. *J Wind Eng Ind Aerodyn* 170:256–273. <https://doi.org/10.1016/j.jweia.2017.08.020>
- Mahnamfar F, Altunkaynak A (2017) Comparison of numerical and experimental analyses for optimizing the geometry of OWC systems. *Ocean Eng* 130:10–24. <https://doi.org/10.1016/j.oceaneng.2016.11.054>
- Manna P, Dharavath M, Sinha PK, Chakraborty D (2013) Optimization of a flight-worthy scramjet combustor through CFD. *Aerosp Sci Technol* 27:138–146. <https://doi.org/10.1016/j.ast.2012.07.005>
- Maurya G, Thandayutham K, Samad A (2022) Effect of fillets on a blade/vane of wave energy harvesting impulse turbine. *Proc Inst Mech Eng Part M J Eng Marit Environ*. <https://doi.org/10.1177/14750902221115948>
- Mohamed MH, Janiga G, Pap E, Thévenin D (2011) Multi-objective optimization of the airfoil shape of Wells turbine used for wave energy conversion. *Energy* 36:438–446. <https://doi.org/10.1016/j.energy.2010.10.021>
- Moñino A, Medina-López E, Clavero M, Benslimane S (2017) Numerical simulation of a simple OWC problem for turbine performance. *Int J Mar Energy* 20:17–32. <https://doi.org/10.1016/j.ijome.2017.11.004>
- Moon YJ, Koh SR (2001) Counter-rotating streamwise vortex formation in the turbine cascade with endwall fence. *Comput Fluids* 30:473–490. [https://doi.org/10.1016/S0045-7930\(00\)00026-8](https://doi.org/10.1016/S0045-7930(00)00026-8)



- Okuhara S, Takao M, Takami A, Setoguchi T (2013) Wells turbine for wave energy conversion—improvement of the performance by means of impulse turbine for bi-directional flow. *Open J Fluid Dyn* 03:36–41. <https://doi.org/10.4236/ojfd.2013.32A006>
- Opoku F, Uddin MN, Atkinson M (2023) A review of computational methods for studying oscillating water columns—the Navier-Stokes based equation approach degree of freedom volume of fluid. *Renew Sustain Energy Rev* 174:113124. <https://doi.org/10.1016/j.rser.2022.113124>
- Raghunathan S (1995) The wells air turbine for wave energy conversion. *Prog Aerosp Sci* 31:335–386. [https://doi.org/10.1016/0376-0421\(95\)00001-F](https://doi.org/10.1016/0376-0421(95)00001-F)
- Raghunathan S, Tan CP (1985) Effect of blade profile on the performance of the Wells self-rectifying air turbine. *Int J Heat Fluid Flow* 6(1):17–22. [https://doi.org/10.1016/0142-727X\(85\)90026-8](https://doi.org/10.1016/0142-727X(85)90026-8)
- Sadees P, Kumar PM, Samad A (2021) Effect of microcylinder and D-cylinder at the leading edge of a wells turbine harvesting wave energy. In: Volume 2B: turbomachinery—axial flow turbine aerodynamics; deposition, erosion, fouling, and icing. American Society of Mechanical Engineers, pp 1–8
- Sadees P, Madhan Kumar P, Samad A (2023) Effect of blade leading-edge microcylinder in a wells turbine used for wave energy converters. *J Ocean Eng Mar Energy* 9:435–453. <https://doi.org/10.1007/s40722-022-00277-4>
- Setoguchi T, Takao M (2006) Current status of self rectifying air turbines for wave energy conversion. *Energy Convers Manag* 47:2382–2396. <https://doi.org/10.1016/j.enconman.2005.11.013>
- Setoguchi T, Kinoue Y, Kim TH et al (2003a) Hysteretic characteristics of wells turbine for wave power conversion. *Renew Energy* 28:2113–2127. [https://doi.org/10.1016/S0960-1481\(03\)00079-X](https://doi.org/10.1016/S0960-1481(03)00079-X)
- Setoguchi T, Santhakumar S, Takao M et al (2003b) A modified wells turbine for wave energy conversion. *Renew Energy* 28:79–91. [https://doi.org/10.1016/S0960-1481\(02\)00006-X](https://doi.org/10.1016/S0960-1481(02)00006-X)
- Shaaban S (2017) Wells turbine blade profile optimization for better wave energy capture. *Int J Energy Res* 41:1767–1780. <https://doi.org/10.1002/er.3745>
- Shaaban S, Hafiz AA (2012) Effect of duct geometry on wells turbine performance. *Energy Convers Manag* 61:51–58. <https://doi.org/10.1016/j.enconman.2012.03.023>
- Shalby M, Elhanafi A, Walker P, Dorrell DG (2019) CFD modelling of a small-scale fixed multi-chamber OWC device. *Appl Ocean Res* 88:37–47. <https://doi.org/10.1016/j.apor.2019.04.003>
- Shehata AS, Xiao Q, Saqr KM et al (2017a) Passive flow control for aerodynamic performance enhancement of airfoil with its application in wells turbine—under oscillating flow condition. *Ocean Eng* 136:31–53. <https://doi.org/10.1016/j.oceaneng.2017.03.010>
- Shehata AS, Xiao Q, Selim MM et al (2017b) Enhancement of performance of wave turbine during stall using passive flow control: first and second law analysis. *Renew Energy* 113:369–392. <https://doi.org/10.1016/j.renene.2017.06.008>
- Taha Z, Sugiyono TY, Sawada T (2011) Numerical investigation on the performance of wells turbine with non-uniform tip clearance for wave energy conversion. *Appl Ocean Res* 33:321–331. <https://doi.org/10.1016/j.apor.2011.07.002>
- Takao M, Thakker A, Abdulhadi R, Setoguchi T (2006) Effect of blade profile on the performance of a large-scale wells turbine for wave-energy conversion. *Int J Sustain Energy* 25:53–61. <https://doi.org/10.1080/14786450600593295>
- Thakker A, Abdulhadi R (2007) Effect of blade profile on the performance of wells turbine under unidirectional sinusoidal and real sea flow conditions. *Int J Rotating Mach* 2007:1–9. <https://doi.org/10.1155/2007/51598>
- Thakker A, Usmani Z, Dhanasekaran TS (2004) Effects of turbine damping on performance of an impulse turbine for wave energy conversion under different sea conditions using numerical simulation techniques. *Renew Energy* 29:2133–2151. <https://doi.org/10.1016/j.renene.2004.03.015>
- Thakker A, Dhanasekaran TS, Ryan J (2005) Experimental studies on effect of guide vane shape on performance of impulse turbine for wave energy conversion. *Renew Energy* 30:2203–2219. <https://doi.org/10.1016/j.renene.2005.02.002>
- Torresi M, Camporeale SM, Pascazio G, Fortunato B (2004) Fluid dynamic analysis of a low solidity wells turbine. In: 59<sup>th</sup> Congr ATI, Genova
- Torresi M, Camporeale SM, Strippoli PD, Pascazio G (2008) Accurate numerical simulation of a high solidity wells turbine. *Renew Energy* 33:735–747. <https://doi.org/10.1016/j.renene.2007.04.006>
- Walker MM, Bons JP (2018) The effect of passive and active boundary-layer fences on swept-wing performance at low reynolds number. *AIAA Aerosp Sci Meet* 2018:1–15. <https://doi.org/10.2514/6.2018-0793>
- Wang Y, Li G, Shen S et al (2018) Investigation on aerodynamic performance of horizontal axis wind turbine by setting micro-cylinder in front of the blade leading edge. *Energy* 143:1107–1124. <https://doi.org/10.1016/j.energy.2017.10.094>
- Xiong C, Liu Z (2011) Numerical analysis on impulse turbine for OWC wave energy conversion. In: Asia-pacific power energy eng conf APPEEC, pp 4–8. <https://doi.org/10.1109/APPEEC.2011.5747685>
- Yang Y, Liu R, Guo R et al (2018) Numerical analysis of underwater flow past columnar projectile with different cross-sections at high Reynolds numbers. *J Vibroeng* 20:1179–1193. <https://doi.org/10.21595/jve.2018.19273>
- Zhong J, Li J, Guo P, Wang Y (2019) Dynamic stall control on a vertical axis wind turbine aerofoil using leading-edge rod. *Energy* 174:246–260. <https://doi.org/10.1016/j.energy.2019.02.176>

**Publisher's Note** Springer Nature remains neutral with regard to jurisdictional claims in published maps and institutional affiliations.

Springer Nature or its licensor (e.g. a society or other partner) holds exclusive rights to this article under a publishing agreement with the author(s) or other rightsholder(s); author self-archiving of the accepted manuscript version of this article is solely governed by the terms of such publishing agreement and applicable law.